Experiments in Fluids (2021) 62:76
https://doi.org/10.1007/s00348-021-03173-z

RESEARCH ARTICLE

Investigation of the atmospheric surface layer using a novel high-resolution sensor array

K. Y. Huang[1] · C. E. Brunner[1] · M. K. Fu[3,4] · K. Kokmanian[1] · T. J. Morrison[2] · A. O. Perelet[2] · M. Calaf[2] · E. Pardyjak[2] · M. Hultmark[1]

Received: 17 November 2020 / Revised: 26 January 2021 / Accepted: 23 February 2021

Abstract

Representing land-atmosphere exchange processes as lower boundary conditions remains a challenge in numerical weather predictions. One important reason is the lack of understanding of heterogeneities in topography, land cover, stability, and their effects on all aspects of the flow field and scalar transport. Well-resolved flow measurements can shed light on these near-surface processes, yielding improved modeling approaches. Yet, it is precisely the heterogeneous characteristics in question—along with the large separation of scales—that make field measurements notoriously challenging. To address some of the difficulties encountered in probing the atmospheric surface layer, a unique and economically scalable field measurement platform was designed around the nanoscale thermal anemometry probe technology, which has previously been used successfully at high Reynolds numbers in laboratory settings. The small size of the nanoscale sensors not only provides a high spatial resolution but also allows for velocity and temperature measurements with the same constant current operating circuit. This operating mode is more economical and straightforward to construct than conventional constant temperature anemometry systems, providing a scalable platform for multi-point measurements. The measurement platform was deployed at the Surface Layer Turbulence and Environmental Science Test site in Utah's West Desert as part of the Idealised horizontal Planar Array study for Quantifying Surface heterogeneity. Streamwise velocity and temperature data were acquired within the first meter above ground with good agreement in spectral behavior to well-known scaling laws in wall-bounded flows.

Graphic Abstract

✉ K. Y. Huang
yichunh@princeton.edu

[1] Princeton University, Princeton, NJ, USA

[2] University of Utah, Salt Lake City, UT, USA

[3] California Institute of Technology, Pasadena, CA, USA

[4] GALCIT, 1200 E California Blvd, Pasadena, CA 91125, USA

1 Introduction

A detailed study of the atmospheric surface layer (ASL)—the region that comprises roughly the lowest tenth of the planetary boundary layer—is imperative on both fundamental and practical grounds. On a fundamental level, the

Published online: 23 March 2021

ASL, under the right conditions, resembles a canonical, thermally stratified turbulent boundary layer and could serve as a naturally high Reynolds number (Re) testing site for wall-bounded turbulence. On a more applied level, the ASL is host to a slew of meteorological phenomena including dew, frost, fog, thermal inversion, and subsidence (Stull 2012) that affect everyday lives and need to be accurately characterized for reliable numerical weather predictions (NWP). A better representation of the velocity, temperature and scalar distribution is needed for realistic lower boundary conditions that shape the near-surface micro-climate.

In recent years, NWP have become indispensable for air-quality control, wind-energy optimization, agriculture, and natural-disaster forecasting. NWP have traditionally parametrized momentum and energy fluxes with ASL similarity theory (Stensrud 2009; ECMWF SP 2014), which is an adequate representation for stationary and planar-homogeneous flows in the absence of subsidence. However, heating and cooling of the land surface together with evaporation and condensation processes modulate turbulent motions within the atmospheric boundary layer throughout its evolution. In other words, thermal and moisture heterogeneities at the surface do not rapidly blend away from the boundary but instead impact the near-surface region of the atmosphere. As a result, multiple studies have indicated a need for improved modeling of surface layer flux-profile relationships that account for these deviations (Ookouchi et al. 1984; Avissar and Schmidt 1998; Seuffert et al. 2002; Desai et al. 2006; Chow et al. 2006; Mironov and Sullivan 2016).

Nevertheless, understanding the dynamics and interactions of near-surface velocity and scalar distributions remains an outstanding challenge in micrometeorology. This is in part due to the difficulties associated with probing the ASL, since near-surface turbulence flux parameterizations necessarily entail well-resolved measurements of the velocity, temperature, and humidity fields and their correlations with each other in the near-surface region.

The challenge with field trials is manifold. Physically, the measurement system needs to be robust and economically scalable. Sensors cannot be fragile as they are often subject to dust, rain, sun, or extreme temperatures. Unlike laboratory studies in which the flow is conditioned and controlled, and a single probe can be traversed for spanwise or wall-normal profiles, field conditions lack homogeneity and statistical stationarity. As such, any study seeking to understand ASL behavior needs to sample multiple locations simultaneously, which drastically increases the number of sensors and operating systems necessary.

Further complicating near-surface field studies is the need for high spatial and temporal resolution. In light of the high Re of atmospheric flows ($Re_\theta \sim O(10^6)$ where θ is the momentum deficit thickness), conventional instrumentation used in atmospheric studies is often neither small nor fast enough to fully resolve the smallest length and time scales in the flow, which are on the order of a millimeter and a millisecond respectively. While Doppler wind lidars are robust and have remarkable range, thus eliminating the need for multiple systems, they are better suited to capture large-scale turbulence, with laser pulses typically 20–80 m long and 10–30 cm in diameter (Tropea and Yarin 2007). For a better representation of the small scales in the flow, sonic anemometers are often used to provide point measurements. While they are robust and simple to operate, they still lack the spatial and temporal resolution necessary to capture the full spectrum of turbulent fluctuations near the surface. Their response to small-scale turbulent fluctuations is limited due to line-averaging along a sampling path (typically ~ 0.1 m) which results in low-pass filtering of the signals. This restriction is exacerbated near surfaces where the scales of motion are extremely small relative to the open path in the sonic, with Wamser et al. (1997) suggesting the minimum measuring height of sonic anemometers as $z_{\min} = 4L$ (where L is the length of the sampling path), or almost half a meter off the ground for most sonic anemometers. Using such instrumentation that filters out the small-scale turbulent fluctuations ultimately leads to bias errors and thus artificially low fluxes.

Even though techniques for measuring turbulent velocity fluctuations accurately and with high resolution are well-known for laboratory environments (Tropea and Yarin 2007), there is often a trade-off between resolution and durability as well as cost and complexity of operation. Even conventional hot-wire anemometers (HWAs) have been employed in only a handful of studies probing the ASL (Kunkel and Marusic 2006; Metzger et al. 2007), as they come with their own set of challenges. In HWA, a metallic filament is heated above flow temperature by the Joule effect. Changes in heat transfer due to flow convection are then registered as resistance changes of the sensor in constant current anemometry (CCA) mode, or as current changes across the sensor in constant temperature anemometry (CTA) and in constant voltage anemometry (CVA) modes. Conventional hot-wires have diameters on the order of 5 µm and are extremely fragile; even a grain of sand carried in the flow can break the wire. Most commercial HWAs operate in CTA mode, in which a feedback loop is used to maintain the wire at a constant temperature, and circuit parameters need to be carefully tuned to achieve high bandwidths (Comte-Bellot 1976). As a result, commercial HWA systems are complex to construct and operate, and quickly become economically demanding for applications requiring multiple probes. Furthermore, calibration in the field is difficult and often requires the use of portable calibration units (Metzger 2003). Recently, a so-called *combo probe* that combines hot-film and sonic anemometry has been developed to facilitate

automated in-situ calibrations using artificial neural network techniques (Kit et al. 2010).

The present set-up seeks to address some of the challenges associated with using HWA in the field by using nanoscale thermal anemometry probes (NSTAPs) instead of conventional hot-wires. The NSTAP has proven effective in capturing small-scale turbulence in numerous laboratory environments (Smits et al. 2011; Ashok et al. 2012; Sinhuber et al. 2015; Bodenschatz et al. 2014; Marusic et al. 2013; Rosenberg et al. 2013; Samie et al. 2018). CCA is not typically used with conventional hot-wires as it yields a relatively low frequency response. However, the small thermal mass of the NSTAP results in inherently small thermal time scales associated with the sensing element, which allow for operation in CCA mode with relatively high frequency response. In CCA, the current is held constant and no feedback loop is required, resulting in operating electronics that are simple to construct from readily available components, bypassing the CTA's complexity and lack of scalability. In addition, the batch manufacturing process of NSTAPs makes them low cost with high repeatability in calibration and performance. Lastly, when sampled simultaneously with the cold-wire version of the NSTAP, named the T-NSTAP, the velocity data can be instantaneously corrected for calibration changes due to changes in ambient temperature. Thus, the unique combination of the NSTAP technology and a CCA mode of operation offers a measurement platform that is high in spatial resolution, easy to construct, economically scalable, and able to account for the drastic ambient temperature changes in the ASL.

As an initial deployment, streamwise velocity and temperature measurements in the first meter above ground were acquired in the deserts of western Utah. The resulting spectra replicated wall-bounded turbulent behaviors that are well-established. The results indicate that the current set-up is able to capture near-surface fluxes accurately and could provide an alternate toolset in the continued quest to explore the ASL.

2 Experimental methods

2.1 Nanoscale sensors

The NSTAP and T-NSTAP are miniature hot- and cold-wires that are capable of measuring velocity and temperature at unprecedented spatiotemporal resolution. Their ability to fully resolve the flow, in turn, guarantees accurate flux measurements. The micro-electromechanical batch manufacturing processes for both sensors are similar and involve metal sputtering and deep-reactive ion etching of a standard 500 µm thick silicon wafer, with each 4-inch diameter wafer producing approximately 180 sensors. As a result, NSTAPs and T-NSTAPs have high degrees of repeatability, are well-behaved in their calibration processes, and are extremely low cost to produce.

The NSTAP is a hot-wire with extremely low thermal mass designed to minimize spatial filtering and end-conduction effects. It consists of a platinum wire filament 100 nm in thickness, 2 µm in width and 60 µm in length suspended on a tapered silicon structure. A simplified 3D representation of the NSTAP is shown in Fig. 1, and scanning electron microscope (SEM) images of the sensing element from both sides are shown in Fig. 2. Platinum was chosen as the sensing element due to its favorable electrical and chemical properties, such as a constant temperature coefficient of resistance over a wide range of temperatures and a good resistance to corrosion and chemical reactions. Bailey et al. (2010) calculated the time response to a step change in velocity of an NSTAP operating in CCA mode to be 50 µs using the local heat balance along a hot-wire probe, compared to a time response of $\sim O(1\,\text{ms})$ in conventional hot-wires.

More recently, the NSTAP design was modified to create the T-NSTAP in order to measure temperature. The T-NSTAP is similar to the NSTAP in geometry and manufacturing process but has a few notable distinctions due to the differing design considerations of hot-wires and cold-wires (Arwatz et al. 2015). In contrast to hot-wires, which are heated and therefore less sensitive to temperature, cold-wires are unheated and adapt to the flow temperature. On the NSTAP, platinum constitutes the bulk of the metal deposit in contact with the silicon support structure (that is, the metal deposit on the silicon other than the freestanding wire itself is also platinum), whereas on the T-NSTAP it is gold, which has a thermal conductivity more than four times that of platinum (Fan et al. 2015). To further ensure that end-conduction effects are minimized, the length of the T-NSTAP wire is 200 µm, which, while longer than that of the NSTAP, is still one order of magnitude shorter than conventional cold-wires. See Fig. 3 for dimensions of the metal trace of the NSTAP and the T-NSTAP.

A comprehensive overview of the NSTAP family of sensors, which also includes the x-NSTAP for two-component velocity measurements and the q-NSTAP for

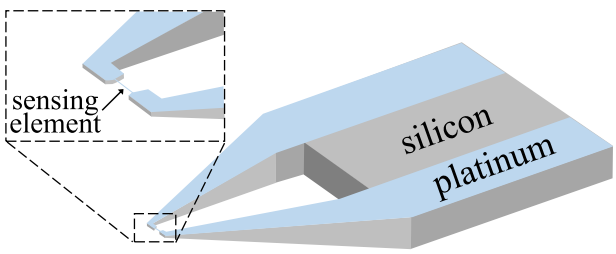

Fig. 1 Simplified schematic of the NSTAP

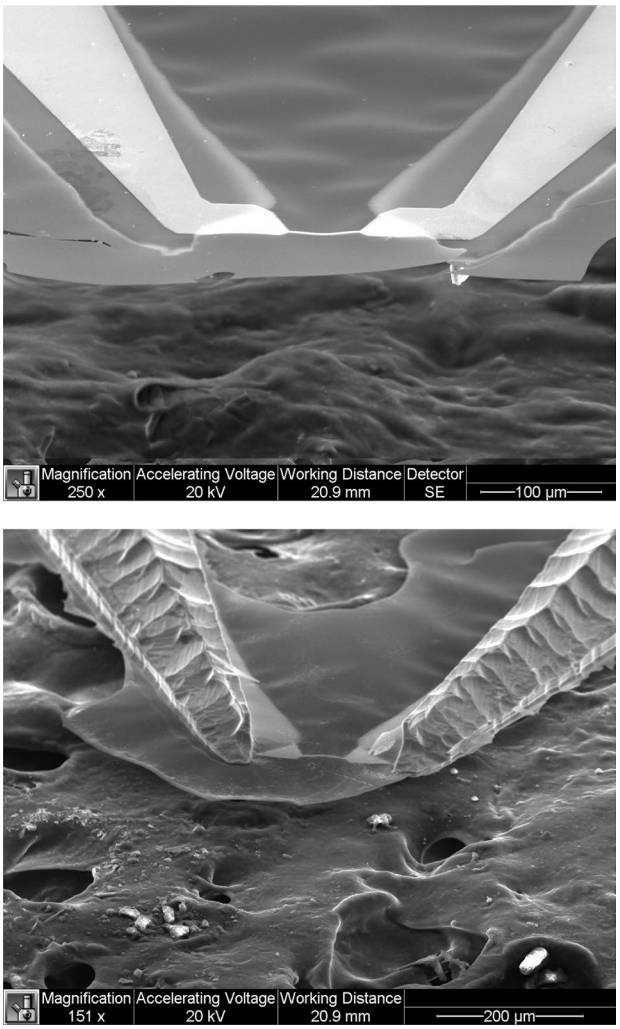

Fig. 2 SEM image of the tip of the NSTAP mounted on carbon tape with the metal side up (top) and the silicon side up (bottom). The SiO_2 film seen in the image is etched away in the final steps of the manufacturing process to create a free-standing wire

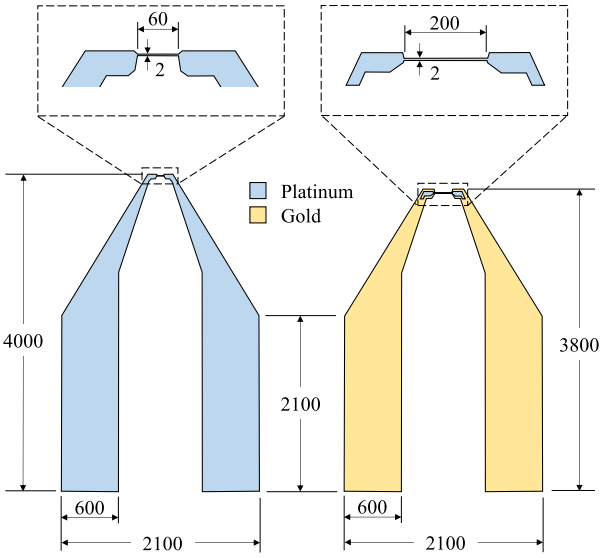

Fig. 3 Metal traces of the NSTAP (left) and the T-NSTAP (right). The dimensions are in µm

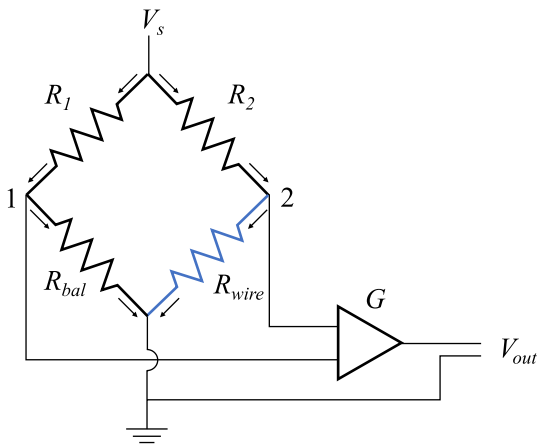

Fig. 4 Simplified schematic of the CCA circuit design, where V_s is the supply voltage, R_1 and R_2 are top resistors of the Wheatstone bridge, R_{bal} is the variable resistor used to balance the bridge output, R_{wire} is the sensor (NSTAP or T-NSTAP), G is the instrument amplifier, and V_{out} is the output voltage

humidity measurements, can be found in Vallikivi and Smits (2014) and Fan et al. (2015).

2.2 CCA circuit design

Both the NSTAP and the T-NSTAP were operated under constant current with the same circuit design, which consists of a Wheatstone bridge with a single-stage amplification of the bridge output. Figure 4 presents a simplified schematic of the design. The Eagle CAD files for the circuit used and the associated parts list are hosted on an open GitHub repository (github.com/d008/CCA).

A stable supply voltage to the bridge is provided by an AC-DC converter (KMD15-1515 from TDK-Lambda Americas) and controlled by a 10 V voltage regulator (AD587 from Analog Devices). The top resistor values (R_1 and R_2) were chosen such that current through the arms of the bridge and thus the sensor (R_{wire}) is low enough that the wire does not exceed its oxidation temperature and break, but still high enough to provide a good response for the desired velocity range. The overheat ratio is $\frac{T_{wire}-T_e}{T_e}$, where T_{wire} is the temperature of the wire in operation and T_e is the temperature of the unheated element. In the current study, for hot-wire operation, the top resistors were 3.3 kΩ, which yields about 3 mA over a typical NSTAP (100–200 Ω). This results in average overheat ratios ranging from 0.29 to 0.37 across the five sampled heights. For cold-wire operation of the

T-NSTAP, the top resistors were 56 kΩ, which yields about 0.2 mA for a typical T-NSTAP (200–300 Ω), so that temperature changes due to Joule heating are negligible. A 200 Ω trimmer potentiometer (R_{bal}) was used to balance and offset the bridge output voltage (V_{out}), measured between nodes 1 and 2 in Fig. 4. Lastly, an instrument amplifier (AD8429 from Analog Devices) with gain $G = 301$ for the NSTAP and $G = 4001$ for the T-NSTAP, was used to boost the signal before collection by the data acquisition system.

The temporal response of the CCA in cold-wire mode is reported to be greater than 10 kHz based on a lumped parameter model that accounts for the effects of end conduction and wire response (Arwatz et al. 2015). For the CCA response in hot-wire mode, Byers et al. (2018) calculated a temporal response of 22 µs in air by numerically solving the balance between Joule heating and convection with an unsteady term to account for the thermal lag. The temporal response was defined as the time it takes for the non-dimensional temperature to decay to $1/e$, where the non-dimensional temperature is the change in wire temperature with respect to an initial condition, $T - T(0)$, divided by the total temperature change of the wire, $T(t \to \infty) - T(0)$. As a conservative estimate, this temporal response translates to a frequency response of approximately 4.5 kHz. Although not necessary for this study and thus not implemented, electronic compensation for the thermal lag in CCA mode, first introduced by Dryden and Kuethe (1929), could be used to achieve an even higher frequency response.

Special care was taken to accommodate the extreme desert heat and solar radiation, as the temperature during the day routinely reaches up to 40°C with no cloud coverage. All electronic components were selected to have high temperature coefficients of resistance, and the custom-printed circuit boards were housed inside metallic boxes outfitted with computer fans to aid in cooling. The circuit box, laptop, and DAQ were all covered with reflective material in an attempt to minimize signal drifts due to temperature changes.

2.3 Experimental set-up

The experiment was carried out at the Surface Layer Turbulence and Environmental Science Test (SLTEST) facility in June 2018 as part of the Idealized horizontal Planar Array experiment for Quantifying Surface heterogeneity (IPAQS). IPAQS included a wide range of surface-layer measurements designed to better understand the impact of surface thermal heterogeneity on near-surface turbulence and mean flow dynamics (Morrison et al. 2021). The SLTEST is a facility in western Utah's Great Salt Lake Desert, which was once the floor of Lake Bonneville. Located within the U.S. Army Dugway Proving Ground, the SLTEST site spans approximately 240 km north-south and 48 km east-west and is characterized by extremely low surface roughness with long uninterrupted fetches of land in the dominant wind directions (see Fig. 5). The smooth surface, which approximates an idealized boundary condition, is naturally renewed every year when the high water table recedes in late spring, leaving behind a stable crust that is very thin and essentially dust free, with an aerodynamic roughness that ranges from less than a millimeter to a couple of millimeters depending on the amount of surface drying and cracking which varies by year and season (Metzger et al. 2007; Jensen et al. 2016). The SLTEST site has been used frequently in the past for high Reynolds number ($Re_\theta \sim O(10^6)$) boundary layer studies due to its near-canonical nature, low velocities, and exceptionally large length scales. A more detailed description of the site can be found in Klewicki et al. (1998), Metzger and Klewicki (2001) and Kunkel and Marusic (2006).

Fig. 5 Image of the SLTEST site, known for its canonical nature due to its low surface roughness, long uninterrupted stretches of land, and regular diurnal wind patterns in early and late summer

Fig. 6 Measurement tower of 1 m height, with acquisition systems placed downwind and covered with reflective material

In this study, five stations of simultaneously sampled NSTAPs and T-NSTAPs were spaced approximately logarithmically within the first meter from the surface, at $z = 0.0625$ m, 0.125 m, 0.25 m, 0.5 m, and 1.0 m (see Fig. 6). However, temperature data at $z = 0.5$ m were not

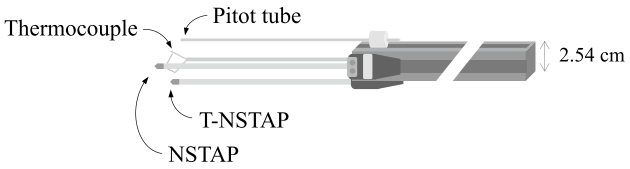

Fig. 7 Schematic of the positioning of sensors at each measurement height. Each sensor is located on one side of a 2.54 cm × 2.54 cm T-slotted aluminum bar, so that there is approximately 3.6 cm between the NSTAP and the T-NSTAP, between the T-NSTAP and the thermocouple, and between the NSTAP and the Pitot tube

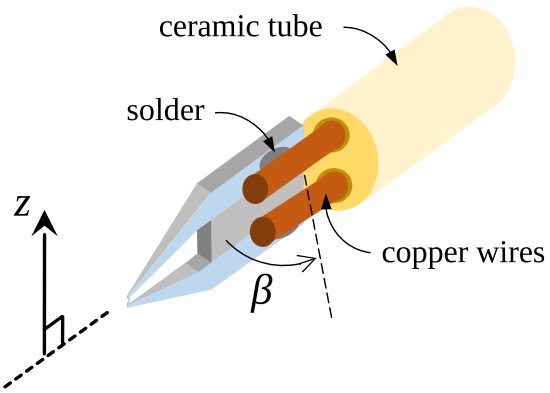

Fig. 8 Schematic of the sensor soldered onto the probe to illustrate the mounting orientation

included in the following analysis since they had unusually high electrical noise levels.

At each sampling height, a 2.54 cm × 2.54 cm T-slotted aluminum bar 30 cm in length was attached to the tower. The individual probes were attached to the aluminum bar using 3D-printed housings (see Fig. 7). Each probe consisted of two copper wires fed through a 2-bore nonporous alumina ceramic tube 2.5 mm in diameter and approximately 10 cm in length. The nanoscale sensors were soldered onto the front ends of the copper wires while the back ends were connected to the CCA circuit using BNC connectors.

For the NSTAP, Fan et al. (2015) reported a deviation in the signal due to non-zero pitch angle β of less than 2% for $-15° \leq \beta \leq 15°$. Following this guideline, the sensors were mounted with the sensing element perpendicular to the ground (see Fig. 8) in order to maximize the wind direction angles that could be accurately captured. The tower was then oriented towards the northwest to align with the dominant wind direction at night. In anticipation of wire breakage, some measurement heights were outfitted with more than one of each sensor. The circuits and acquisition system were placed downwind of the tower to minimize flow disturbances. Although they could certainly be sampled at higher frequencies, the sensors were sampled at 100 Hz for this initial deployment.

2.4 Calibration

At each measurement height, one Pitot tube and one thermocouple were also mounted to provide in-situ mean values for calibration of the nanoscale sensors. The Pitot tube had an inner diameter of 1/16" and was sampled at 100 Hz using a Honeywell pressure sensor (TruStability® HSC with 250 Pa range at ±0.25% accuracy). The thermocouple was an E-type fine-wire of 25.4 µm diameter and was sampled at 10 Hz.

2.4.1 T-NSTAP

The sensor resistance R_{wire} is first calculated with the Wheatstone bridge relations using the circuit values given in sect. 2.2. A linear relationship between R_{wire} and the wire temperature in operation T_{wire} was then prescribed following Hultmark and Smits (2010) such that

$$T_{\text{wire}} = T_{\text{ref}} + \frac{1}{\alpha}\left(\frac{R_{\text{wire}}}{R_{\text{ref}}} - 1\right) \tag{1}$$

where R_{ref} is the resistance of the wire taken at a reference temperature T_{ref}, and α is the temperature coefficient of resistance of the wire ($\alpha = 0.0019\,\text{K}^{-1}$). The thermocouple was used to obtain T_{ref} prior to data acquisition.

2.4.2 NSTAP

Calibration of hot-wires, conventionally carried out in controlled facilities such as wind tunnels, proves a challenge in the field. One solution is to use a portable calibration unit consisting of a miniature open-return wind tunnel for pre- and post-calibration in the field (Metzger et al. 2007). However, to further simplify the calibration procedure, and to reduce sensor breakage associated with moving nanoscale sensors in and out of the calibration unit, the current study instead used attached Pitot tubes adjacent to each NSTAP to provide continuous, in-situ mean velocity data.

Before the calibration curve was determined, temperature compensation was carried out to address one of the main sources of error in HWA – the change in calibration due to changes in ambient temperature (Bruun 1996). This problem is particularly important in field conditions, where the ambient temperature cannot be controlled and varies drastically throughout the day. The current set-up with simultaneous velocity and temperature measurements makes it perfectly suited for an instantaneous application of the temperature compensation scheme proposed by Hultmark and Smits (2010). To accurately capture the effects of changing temperature on the calibration in CCA mode, they proposed the relationship between streamwise velocity (U) and the voltage across the wire in operation (E) to be

$$\frac{U}{\nu} = f\left(\frac{E}{k\Delta T}\right) \tag{2}$$

where ν is the fluid kinematic viscosity, k is the fluid thermal conductivity, and ΔT is the temperature difference between the hot-wire and the surrounding fluid (i.e. $\Delta T = T_{\text{wire}} - T_{\text{ambient}}$). Equation (1) was used to calculate the temperature of the hot-wire, and k and ν were evaluated at the average temperature between that of the hot-wire and ambient air (known as the film temperature) using the correlation given by Kannuluik and Carman (1951) for air. The flow velocity was provided by the Pitot tube. After applying the temperature compensation scheme, a King's Law fit was applied to relate U/ν to $E/k\Delta T$.

Fig. 9 shows a sample calibration curve for the NSTAP located at $z = 0.125$ m before and after applying the temperature compensation scheme. The data nearly collapse to a single curve after temperature compensation, demonstrating that the correction technique was able to capture the effects of changing ambient temperature.

2.5 Data uncertainty

Uncertainty in the data arises mainly from two sources: the propagation of systematic instrumentation errors and incomplete convergence due to the limited sampling time. Systematic errors obtained with the NSTAP and its calibration procedure were calculated following Yavuzkurt (1984). Uncertainty from lack of convergence was estimated from the theoretical ensemble-average difference as described by Wyngaard (1992) for a 30-minute sampling period. The estimated total error accounting for both systematic and incomplete convergence for each sampling height averaged over the hour of study is presented in Table 1.

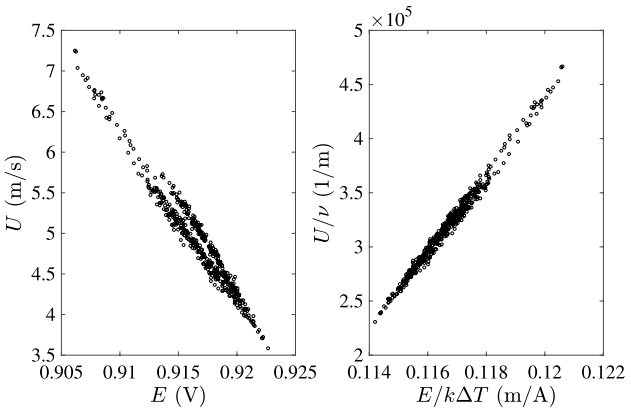

Fig. 9 Calibration curves before (left) and after (right) temperature compensation at $z = 0.125$ m. Each data point represents an average value over 15 s

Table 1 Estimated total error

z (m)	z (%)	U (%)	$\overline{u'^2}$ (%)	T (%)	$\overline{T'^2}$ (%)
0.0625	3.2	6.7	11.5	6.1	10.8
0.125	1.6	6.5	11.0	6.1	10.6
0.25	0.8	7.5	12.6	6.1	10.7
0.5	0.4	10.4	18.0	–	–
1	0.2	13.4	24.3	6.1	10.6

Sampling heights were measured using a tape measure with an uncertainty of ±2 mm. For U, the uncertainty in the NSTAP at the lowest three heights is on the same order as those reported by Kunkel and Marusic (2006). However, the sensors at $z = 0.5$ m and 1 m suffered higher instrument error. This could be due to misalignment between the pitch of the Pitot tube and the NSTAP. For $\overline{u'^2}$, the estimated total errors at all heights except $z = 1$ m are consistent with other studies of the same site (Kunkel and Marusic 2006; Metzger et al. 2007). The T-NSTAP exhibited a total estimated error of around 6% for T and around 11% for $\overline{T'^2}$ at all sampling heights.

3 Mean flow parameters

The present study focuses on the one-hour period soon after sunset on June 21st since both near-neutral stability and wind-alignment with the sensors occurred during this time frame. Both of these criteria are verified by a nearby sonic anemometer (Campbell Scientific CSAT3) stationed approximately 10 m west at a height of 2 m.

The hour-long timeframe was split into two 30-minute periods, and trends caused by a varying freestream velocity are removed following the methodology of Hutchins et al. (2012). Assumed and calculated mean flow parameters for each period are given in Table 2. Data from the nearby sonic anemometer sampled at 20 Hz, along with an adjacent fine-wire K-type thermocouple and humidity sensor (Vaisala HMP60), were used to calculate half-hourly mean values following planar fit of the wind direction. Using standard methods as described in Stull (2012), these mean quantities include the friction velocity taken to be

$$u_* = (-\overline{u'w'})^{1/2}, \tag{3}$$

the characteristic ASL turbulent temperature scale

$$\theta_* = -\frac{\overline{w'\theta'_v}}{u_*}, \tag{4}$$

and the Obukhov length scale

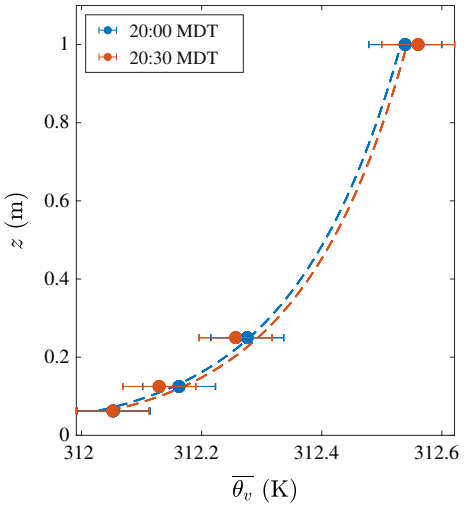

Fig. 10 Mean virtual potential temperature profile. The dashed lines correspond to $\psi_H = 0.74$

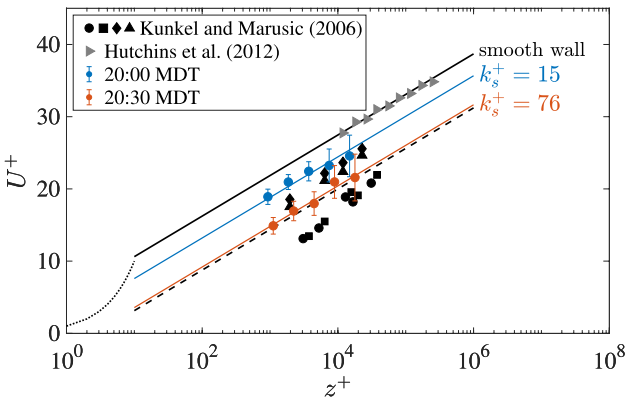

Fig. 11 Mean streamwise velocity profile. The solid black line indicates the relation for a smooth wall, the dashed line for an equivalent sand grain roughness value of $k_s^+ = 90$ (above which the wall is considered fully rough), and the dotted line for the viscous region. Solid black symbols correspond to the four experimental runs in Kunkel and Marusic (2006) and solid grey symbols are from Hutchins et al. (2012)

$$L = -\frac{u_*^3}{\kappa \frac{g}{\theta_v} \overline{w'\theta_v'}}, \tag{5}$$

where u' and w' denote streamwise and vertical velocity fluctuations respectively, $\kappa = 0.41$ is the von Kármán constant, g is the gravitational acceleration, and θ_v is the virtual potential temperature. The viscous or inner unit of length is represented by the quantity ν/u_*.

The stability parameter $\zeta = z/L$ characterizes the thermal stability of the ASL, with $\zeta < 0$ indicating an unstable ASL (such as over land during day time), $\zeta > 0$ a stable ASL (such as over land at night), and $\zeta \cong 0$ (usually $|\zeta| \leq 0.1$) a near-neutral ASL. Further, the mean virtual potential temperature profile captured by the T-NSTAP (see Fig. 10) is well-described by the near-neutral value of 0.74 for the Monin-Obukhov similarity function $\psi_H = \frac{\kappa z}{\theta_*} \frac{\partial \overline{\theta_v}}{\partial z}$ (Stull 2012).

The mean streamwise velocities measured from the NSTAP as a function of distance from the surface in inner coordinates are plotted in Fig. 11 for the two 30-minute periods. The data generally follow the logarithmic relation as expected in this region, with an offset due to roughness. To find the equivalent sand grain roughness height k_s, the mean streamwise velocity profiles were fitted with the generally accepted relation for a zero-pressure gradient neutral boundary layer

$$U^+ = \frac{1}{\kappa} \ln\left[\frac{z}{k_s}\right] + B, \tag{6}$$

where U is the mean axial velocity at a distance z from the wall, k_s is the equivalent sand grain roughness height, B is a function of the roughness height, and the superscript + denotes inner normalization by u_* for velocity and by ν/u_* for length (Schlichting 1968). Ligrani and Moffat (1986) show for hydrodynamically smooth walls ($k_s^+ < 2.25$)

$$B = \frac{1}{\kappa} \ln\left[k_s^+\right] + A, \tag{7}$$

where $A = 5.0$ is a constant; for fully rough walls ($k_s^+ > 90$)

$$B = 8.5; \tag{8}$$

and for the transitional region between the two regimes ($2.25 \leq k_s^+ \leq 90$)

$$B = \frac{1}{\kappa} \ln\left[k_s^+\right] + A + \left(8.5 - A - \frac{1}{\kappa} \ln\left[k_s^+\right]\right) \sin\left[\frac{1}{2}\pi h\right], \tag{9}$$

where

$$h = \frac{\ln\left[k_s^+/2.25\right]}{\ln\left[90/2.25\right]}. \tag{10}$$

The equivalent sand grain roughness heights are on the same order as those reported by Kunkel and Marusic (2006), and slightly higher than those reported by Hutchins et al. (2012), as shown in Fig. 11. This variation could be due to the natural degradation of the desert surface as it dries and cracks over the course of the summer, the process of which varies from year to year.

The surface roughness can also be quantified in terms of the aerodynamic roughness length z_0, defined such that

$$U^+ = \frac{1}{\kappa} \ln\left[\frac{z}{z_0}\right]. \tag{11}$$

The surface-layer depth δ is estimated to be 60 m based on comparisons of $\overline{u'^2}$ profiles with studies of the same site and

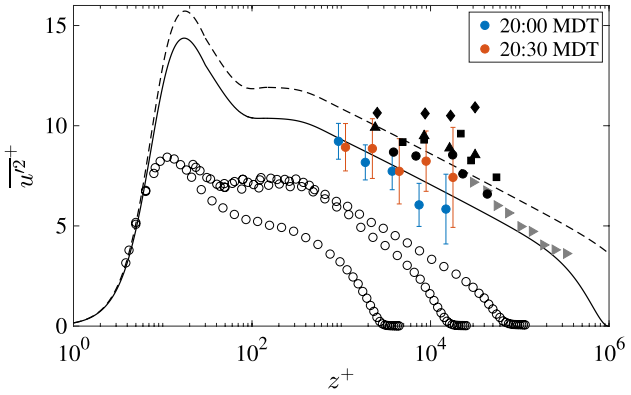

Fig. 12 Streamwise turbulence intensities. The solid line indicates the relation by Marusic and Kunkel (2003) at $Re_\tau = 1 \times 10^6$ and the dashed line at $Re_\tau = 3.8 \times 10^6$. The open circles are laboratory boundary layer data from Vallikivi et al. (2015) at $Re_\tau = 3 \times 10^3$, 1.5×10^4, and 7×10^4; the solid symbols are the same as in Fig. 11

the similarity formulations proposed by Marusic and Kunkel (2003). This yields $Re_\tau \approx 1 \times 10^6$ for the current data set. Profiles of $\overline{u'^2}$ are presented in Fig. 12, along with atmospheric data from Kunkel and Marusic (2006) and Hutchins et al. (2012), and laboratory data from Vallikivi et al. (2015).

Lastly, to provide an estimate for the physical size of eddies encountered, the one-hour averaged streamwise integral length scale L_u^x, the Taylor microscale λ, and the Kolmogorov length scale η were calculated and presented in Fig. 13. The integral length scale L_u^x was calculated from integration of the temporal autocorrelation function and is on the same order as those reported by Emes et al. (2019) for the same site under near-neutral stability conditions. The Taylor microscale λ was calculated using two approaches, one based on the osculating parabola of the temporal autocorrelation function at zero time lag, and the other based on the assumption of isotropic turbulence such

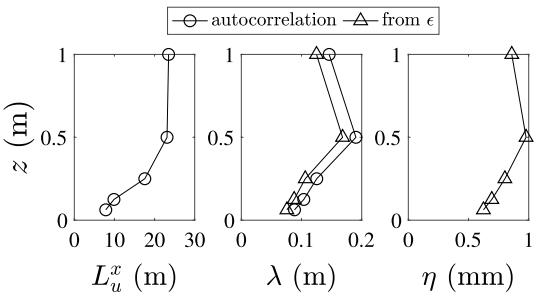

Fig. 13 Vertical profiles of the streamwise integral length scale L_u^x, the Taylor microscale λ, and the Kolmogorov length scale η averaged over the sampling period of 2000 – 2100 MDT on 21 June 2018

that $\lambda = \sqrt{15\frac{\nu\overline{u'^2}}{\epsilon}}$, where ϵ is the mean turbulent kinetic energy dissipation rate estimated as

$$\epsilon = 15\nu \int_0^\infty k^2 \phi_{uu}(k) dk. \tag{12}$$

The Kolmogorov length scale η, defined as $\eta = \left(\frac{\nu^3}{\epsilon}\right)^{1/4}$, was calculated using the estimate for ϵ given above. Additional information regarding the formulations can be found in Pope (2001).

4 Results

To quantify the performance of the experimental set-up, spectral analysis of the measurements was performed in time using standard fast-Fourier-transform methods with an averaging interval of 15 minutes per run. The presented spectra have been smoothed using a binning method to better illustrate the underlying features, and a constant level of electronic noise has been subtracted. Taylor's frozen field hypothesis was applied to transform the spectra from frequency (f) to wavenumber (k) space, where $k = \frac{2\pi f}{\overline{U}}$ and $\overline{U}$ is the mean streamwise velocity.

4.1 Streamwise velocity spectra

The streamwise velocity spectra ϕ_{uu} in inner coordinates are shown in Fig. 14 and exhibit the two well-known scaling behaviors, with almost two decades of k^{-1} scaling (at the smallest z^+ sampled) and an extended length of the inertial subrange with a $k^{-5/3}$ behavior. The transition between these two regimes occurs roughly at $kz \sim 1$, consistent with the attached-eddy model of wall turbulence and the spectral theory introduced by Katul et al. (2012).

Table 2 Mean flow parameters

	21 June 2018	
	20:00 MDT	20:30 MDT
wind direction (°)	321	316
δ (m)	60	60
u_* (m/s)	0.24	0.29
ν/u_* (mm)	0.067	0.056
L (m)	36.0	52.2
ζ at 1 m	0.028	0.019
θ_* (K)	0.10	0.10
k_s (mm)	0.98	4.26
z_0 (mm)	0.03	0.13

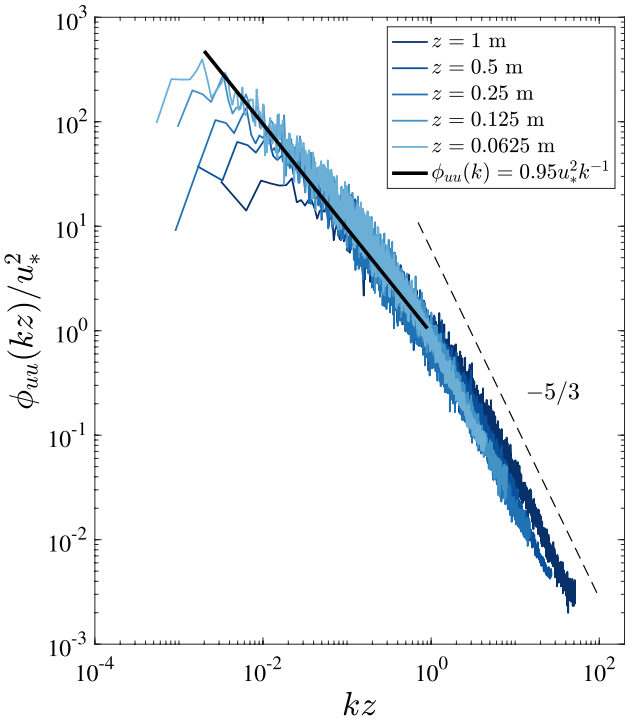

Fig. 14 Inner-normalized streamwise velocity spectra for NSTAP measurements at five different heights during the sampling period of 2000 − 2100 MDT on 21 June 2018

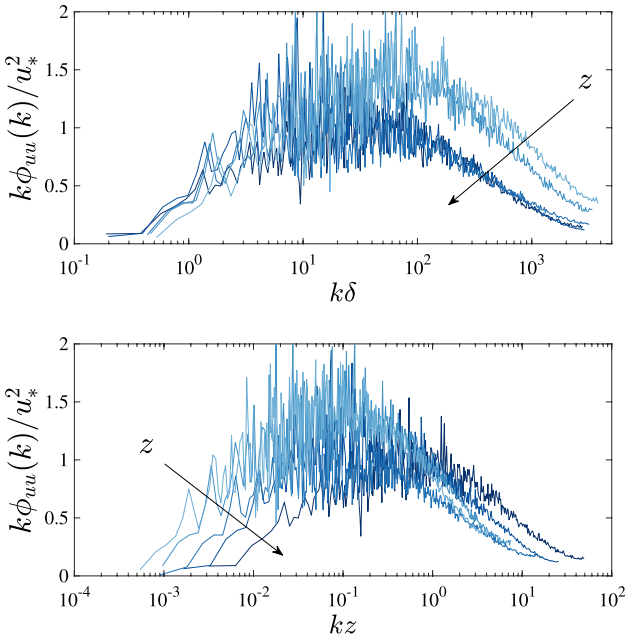

Fig. 15 Premultiplied streamwise velocity spectra normalized with outer flow scaling (top) and with distance from the wall (bottom) from the same time period and with the same legend as in Fig. 14

The k^{-1} scaling behavior in the energy-containing range has been conjectured from dimensional analysis (Kader and Yaglom 1991; Katul et al. 1995b), from simplified spectral budgets (Tchen 1953, 1954; Katul et al. 2012; Banerjee and Katul 2013; Banerjee et al. 2015), and from asymptotic matching between the inner and outer regions of the boundary layer (Perry and Abell 1975, 1977; Perry et al. 1986, 1994). Despite ample theoretical prediction, the existence of the k^{-1} law remains somewhat of a controversy since it has not always been observed experimentally, even in high-*Re* flows (Morrison et al. 2002). Nickels et al. (2005) proposed that to ensure an overlap region and subsequently see an extended k^{-1} scaling law, *Re* must be sufficiently large ($\delta^+ \geq$ 52,500), z^+ sufficiently large ($z^+ \geq 100$), and z/δ sufficiently small ($z/\delta \leq$0.019). All three criteria are met in the present study. Furthermore, as discussed by Kader and Yaglom (1991), $\phi_{uu} = C_u u_*^2 k^{-1}$, where $0.9 \leq C_u \leq 1$. The current data set is well-approximated by $C_u = 0.95$ in the k^{-1} region.

Overall, the log-log representation of the streamwise velocity spectra exhibits the expected $k^{-5/3}$ scaling in the inertial region and displays the elusive k^{-1} region in lower wavenumbers, consistent with other atmospheric studies (Kunkel and Marusic 2006; Calaf et al. 2013; Hultmark et al. 2013).

The spectra are also plotted in premultiplied form with additional smoothing using both outer normalization and normalization using distance from the wall in Fig. 15. The premultiplied form is useful in examining the existence of the k^{-1} scaling since the region will appear as a plateau, and the area under the spectra corresponds to the overall energy level. According to the attached-eddy model (Perry and Li 1990), spectra in the outer flow scaling region should collapse at low k and in the k^{-1} region, and should peel off with z/δ at high k. With distance-from-the-wall scaling, the spectra should collapse at non-dimensional wavenumbers corresponding to the k^{-1} and $k^{-5/3}$ overlap regions, and peel off at wavenumbers lower than the k^{-1} region. The data in this study generally conform to the expected behavior, with the scatter possibly due to non-stationarity or limited sampling times.

4.2 Temperature spectra

The one-dimensional temperature spectra are plotted in Fig. 16 and shifted by an arbitrary offset in Fig. 17 to examine them individually. The temperature spectra exhibit an extensive k^{-1} scaling region at low k, which has also been observed in other ASL field experiments under near-neutral, mildly stable/unstable conditions (Kader and Yaglom 1991; Katul et al. 1995b; Li et al. 2015), and theorized from the z-independence argument (Kader and Yaglom 1991) and more recently from simplified spectral budgets (Li et al. 2016). Furthermore, Kader and Yaglom (1991) and Katul et al. (1995a) showed that under

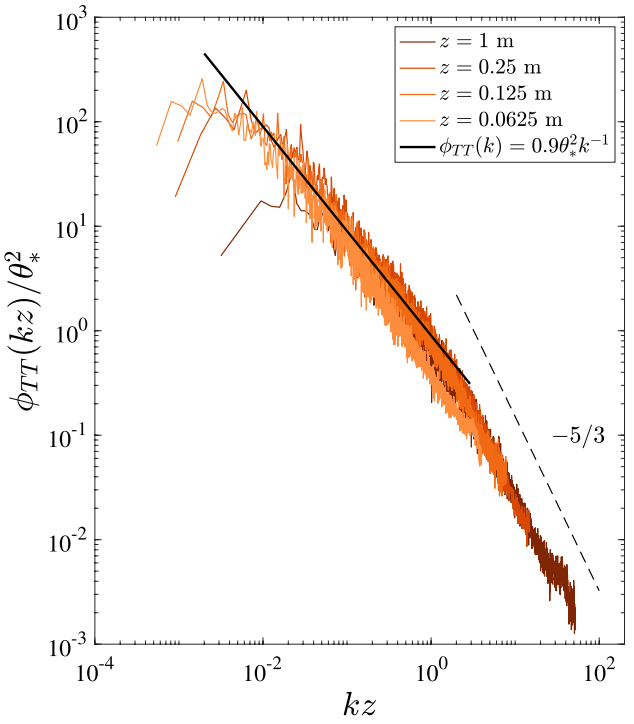

Fig. 16 1D temperature spectra in wavenumber space from the same time period as in Fig. 14

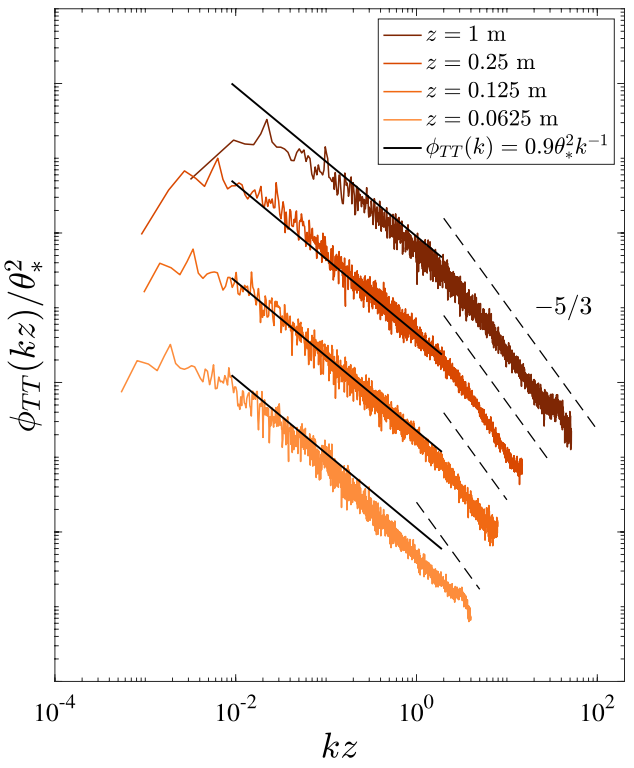

Fig. 17 1D temperature spectra in wavenumber space, with arbitrary offsets to distinguish the behavior at different heights, from the same time period as in Fig. 14

near-neutral conditions, $\phi_{TT} \approx 0.9\theta_*^2 k^{-1}$. This relation is plotted in Fig. 17 for each height, and appears to characterize the low-wavenumber behavior well. The $k^{-5/3}$ inertial-range behavior of the temperature spectra has been extensively studied (Kaimal et al. 1972; Wyngaard and Coté 1972; Kaimal 1973). In the present study, its extent increased with height for the highest two heights. The lack of $k^{-5/3}$ scaling behavior at the lowest height could be due to low Reynolds number effects, anisotropy, or the limited sampling frequency (100 Hz). Similar trends have also been observed in laboratory studies at high Reynolds numbers (Vallikivi et al. 2015).

5 Conclusions and future use

The crux of the measurement platform presented in this paper lies in the use of nanoscale thermal anemometry probes, whose high spatial resolution exceeds that of the smallest scales in atmospheric flow and allows for operation in constant current anemometry (CCA) mode. While CCA has slower time responses compared to constant voltage or constant temperature methods due to thermal lag, the low cost and simplicity of the electronic system allow for distributed deployment of the sensors in large arrays. This is an important advantage especially in field experiments where multiple measurement locations and systems are needed to account for the variability in surface heterogeneity.

The present study describes a limited initial deployment that captures streamwise velocity and temperature measurements simultaneously in the first meter from the surface. The results demonstrate that the instrumentation array works well by comparison against well-known wall-bounded turbulence predictions. The array was able to reproduce the elusive k^{-1} behavior and also show inertial-range behavior that agrees with observations in other studies. The promising results indicate the viability of the current set-up as an alternate toolset for probing the atmospheric surface layer.

For future studies, the flexibility of the set-up along with the range of nanoscale sensors in the NSTAP family (Fan et al. 2015) provide the means to investigate various turbulence phenomena in the ASL. For two-component velocity fluctuations, either x-NSTAPs or two NSTAPs mounted at 90 degrees to each other could be used. This eliminates the need for sonic anemometers for vertical velocity measurements, and, in conjunction with T-NSTAPs, could give insight into wall-normal thermal fluxes near the surface. The q-NSTAP offers humidity measurements with extremely high bandwidth (≈ 500 kHz) and high spatial resolution (≈ 0.1 μm in thickness), much higher than any state of the science humidity sensors. It could be deployed in an array

along with two-component velocity measurement sensors to quantify latent heat fluxes at unprecedented scales. With a horizontal rake, spanwise spectra can be captured which could give insight into turbulent structures. Finally, deployment of a 3D array of sensors could enable a comprehensive study of the spatial structure and heterogeneity of surface fluxes over natural terrain. The wide range of turbulence quantities that could be studied with the set-up would aid in quantifying and representing land-atmosphere exchange processes.

Acknowledgements This work was supported by the NSF AGS-1649049 (Program manager: Dr. JS). KYH and CEB were supported by the Department of Defense (DoD) through the National Defense Science and Engineering Graduate Fellowship (NDSEG) Program. The authors would like to thank Prof. Clayton Byers and Agastya Parikh for their assistance with the CCA circuit design, Alexander Piqué for providing support in the field, and Princeton University's clean room staff for their assistance in manufacturing the sensors.

References

Arwatz G, Fan Y, Bahri C, Hultmark M (2015) Development and characterization of a nano-scale temperature sensor (T-NSTAP) for turbulent temperature measurements. Meas Sci Technol 26(3):035103

Ashok A, Bailey SCC, Hultmark M, Smits AJ (2012) Hot-wire spatial resolution effects in measurements of grid-generated turbulence. Exp fluids 53(6):1713–1722

Avissar R, Schmidt T (1998) An evaluation of the scale at which ground-surface heat flux patchiness affects the convective boundary layer using large-eddy simulations. J Atmos Sci 55(16):2666–2689

Bailey SCC, Kunkel GJ, Hultmark M, Vallikivi M, Hill JP, Meyer KA, Tsay C, Arnold CB, Smits AJ (2010) Turbulence measurements using a nanoscale thermal anemometry probe. J Fluid Mech 663:160–179

Banerjee T, Katul GG (2013) Logarithmic scaling in the longitudinal velocity variance explained by a spectral budget. Phys Fluids 25(12):125106

Banerjee T, Katul GG, Salesky ST, Chamecki M (2015) Revisiting the formulations for the longitudinal velocity variance in the unstable atmospheric surface layer. Quart J R Meteorol Soc 141(690):1699–1711

Bodenschatz E, Bewley GP, Nobach H, Sinhuber M, Xu H (2014) Variable density turbulence tunnel facility. Rev Sci Instrum 85(9):093908

Bruun HH (1996) Hot-wire anemometry: principles and signal analysis. IOP Publishing, Bristol

Byers CP, Fu MK, Fan Y, Hultmark M (2018) Development of instrumentation for measurements of two components of velocity with a single sensing element. Meas Sci Technol 29(2):025304

Calaf M, Hultmark M, Oldroyd HJ, Simeonov V, Parlange MB (2013) Coherent structures and the k^{-1} spectral behaviour. Phys Fluids 25(12):125107

Chow FK, Weigel AP, Street RL, Rotach MW, Xue M (2006) High-resolution large-eddy simulations of flow in a steep Alpine valley. J Appl Meteorol Climatol 45(1):63–86

Comte-Bellot G (1976) Hot-wire anemometry. Annu Rev Fluid Mech 8(1):209–231

Desai AR, Davis KJ, Senff CJ, Ismail S, Browell EV, Stauffer DR, Reen BP (2006) A case study on the effects of heterogeneous soil moisture on mesoscale boundary-layer structure in the southern Great Plains, USA. Bound Layer Meteorol 119(2):195–238

Dryden HL, Kuethe AM (1929) The measurement of fluctuations of air speed by the hot-wire anemometer. US Government Printing Office

ECMWF SP, (2014) IFS documentation CY40R1 part IV: Physical processes. ECMWF, Reading, UK, pp 111–113

Emes MJ, Arjomandi M, Kelso RM, Ghanadi F (2019) Turbulence length scales in a low-roughness near-neutral atmospheric surface layer. J Turbul 20(9):545–562

Fan Y, Arwatz G, Van Buren TW, Hoffman DE, Hultmark M (2015) Nanoscale sensing devices for turbulence measurements. Exp Fluids 56(7):138

Hultmark M, Smits AJ (2010) Temperature corrections for constant temperature and constant current hot-wire anemometers. Meas Sci Technol 21(10):105404

Hultmark M, Vallikivi M, Bailey SCC, Smits AJ (2013) Logarithmic scaling of turbulence in smooth-and rough-wall pipe flow. J Fluid Mech 728:376–395

Hutchins N, Chauhan K, Marusic I, Monty J, Klewicki J (2012) Towards reconciling the large-scale structure of turbulent boundary layers in the atmosphere and laboratory. Bound Layer Meteorol 145(2):273–306

Jensen DD, Nadeau DF, Hoch SW, Pardyjak ER (2016) Observations of near-surface heat-flux and temperature profiles through the early evening transition over contrasting surfaces. Bound Layer Meteorol 159(3):567–587

Kader BA, Yaglom AM (1991) Spectra and correlation functions of surface layer atmospheric turbulence in unstable thermal stratification. In: Turbulence and Coherent Structures. Fluid Mechanics and Its Applications, vol 2. Springer, Dordrecht

Kaimal JCJ (1973) Turbulenece spectra, length scales and structure parameters in the stable surface layer. Bound Layer Meteorol 4(1–4):289–309

Kaimal JCJ, Wyngaard JC, Izumi Y, Coté OR (1972) Spectral characteristics of surface-layer turbulence. Quart J R Meteorol Soc 98(417):563–589

Kannuluik WG, Carman EH (1951) The temperature dependence of the thermal conductivity of air. Aust J Chem 4(3):305–314

Katul GG, Chu CR, Parlange MB, Albertson JD, Ortenburger TA (1995a) Low-wavenumber spectral characteristics of velocity and temperature in the atmospheric surface layer. J Geophys Res Atmos 100(D7):14243–14255

Katul GG, Goltz SM, Hsieh CI, Cheng Y, Mowry F, Sigmon J (1995b) Estimation of surface heat and momentum fluxes using the flux-variance method above uniform and non-uniform terrain. Bound Layer Meteorol 74(3):237–260

Katul GG, Porporato A, Nikora V (2012) Existence of k^{-1} power-law scaling in the equilibrium regions of wall-bounded turbulence explained by Heisenberg's eddy viscosity. Phys Rev E 86(6):066311

Kit E, Cherkassky A, Sant T, Fernando HJS (2010) In situ calibration of hot-film probes using a collocated sonic anemometer: Implementation of a neural network. J Atmos Ocean Technol 27(1):23–41

Klewicki JC, Foss JF, Wallace JM (1998) High Reynolds number [$R_\theta = O(10^6)$] boundary layer turbulence in the atmospheric surface layer above western Utah's salt flats. In: Flow at Ultra-High Reynolds and Rayleigh Numbers. Springer, New York

Kunkel GJ, Marusic I (2006) Study of the near-wall-turbulent region of the high-Reynolds-number boundary layer using an atmospheric flow. J Fluid Mech 548:375–402

Li D, Katul GG, Bou-Zeid E (2015) Turbulent energy spectra and cospectra of momentum and heat fluxes in the stable atmospheric surface layer. Bound Layer Meteorol 157(1):1–21

Li D, Katul GG, Gentine P (2016) The k^{-1} scaling of air temperature spectra in atmospheric surface layer flows. Quart J R Meteorol Soc 142(694):496–505

Ligrani PM, Moffat RJ (1986) Structure of transitionally rough and fully rough turbulent boundary layers. J Fluid Mech 162:69–98

Marusic I, Kunkel GJ (2003) Streamwise turbulence intensity formulation for flat-plate boundary layers. Phys Fluids 15(8):2461–2464

Marusic I, Monty JP, Hultmark M, Smits AJ (2013) On the logarithmic region in wall turbulence. J Fluid Mech 716:R3

Metzger MM (2003) Scalar dispersion in high Reynolds number turbulent boundary layers. PhD thesis, University of Utah

Metzger MM, Klewicki JC (2001) A comparative study of near-wall turbulence in high and low Reynolds number boundary layers. Phys Fluids 13(3):692–701

Metzger MM, McKeon BJ, Holmes H (2007) The near-neutral atmospheric surface layer: turbulence and non-stationarity. Philos Trans R Soc A Math Phys Eng Sci 365(1852):859–876

Mironov DV, Sullivan PP (2016) Second-moment budgets and mixing intensity in the stably stratified atmospheric boundary layer over thermally heterogeneous surfaces. J Atmos Sci 73(1):449–464

Morrison JF, Jiang W, McKeon BJ, Smits AJ (2002) Reynolds number dependence of streamwise velocity spectra in turbulent pipe flow. Phys Rev Lett 88(21):214501

Morrison T, Calaf M, Higgins C, Drake SA, Perelet A, Pardyjak E (2021) The impact of surface temperature heterogeneity on near-surface heattransport, Boundary-Layer Meteor. accepted

Nickels TB, Marusic I, Hafez S, Chong MS (2005) Evidence of the k_1^{-1} law in a high-Reynolds-number turbulent boundary layer. Phys Rev Lett 95(7):074501

Ookouchi Y, Segal M, Kessler RC, Pielke RA (1984) Evaluation of soil moisture effects on the generation and modification of mesoscale circulations. Mon Weather Rev 112(11):2281–2292

Perry AE, Abell CJ (1975) Scaling laws for pipe-flow turbulence. J Fluid Mech 67(2):257–271

Perry AE, Abell CJ (1977) Asymptotic similarity of turbulence structures in smooth-and rough-walled pipes. J Fluid Mech 79(4):785–799

Perry AE, Li JD (1990) Experimental support for the attached-eddy hypothesis in zero-pressure-gradient turbulent boundary layers. J Fluid Mech 218:405–438

Perry AE, Henbest S, Chong MS (1986) A theoretical and experimental study of wall turbulence. J Fluid Mech 165:163–199

Perry AE, Marusic I, Li JD (1994) Wall turbulence closure based on classical similarity laws and the attached eddy hypothesis. Phy Fluids 6(2):1024–1035

Pope SB (2001) Turbulent flows. IOP Publishing, Bristol

Rosenberg BJ, Hultmark M, Vallikivi M, Bailey SCC, Smits AJ (2013) Turbulence spectra in smooth-and rough-wall pipe flow at extreme Reynolds numbers. J Fluid Mech 731:46–63

Samie M, Marusic I, Hutchins N, Fu MK, Fan Y, Hultmark M, Smits AJ (2018) Fully resolved measurements of turbulent boundary layer flows up to $Re_\tau = 20000$. J Fluid Mech 851:391–415

Schlichting H (1968) Boundary layer theory, vol 960. Springer, Berlin

Seuffert G, Gross P, Simmer C, Wood EF (2002) The influence of hydrologic modeling on the predicted local weather: Two-way coupling of a mesoscale weather prediction model and a land surface hydrologic model. J Hydrometeorol 3(5):505–523

Sinhuber M, Bodenschatz E, Bewley GP (2015) Decay of turbulence at high R eynolds numbers. Phys Revi Lett 114(3):034501

Smits AJ, McKeon BJ, Marusic I (2011) High-Reynolds number wall turbulence. Annu Rev Fluid Mech 43:418–428

Stensrud DJ (2009) Parameterization schemes: keys to understanding numerical weather prediction models. Cambridge University Press, Cambridge

Stull RB (2012) An introduction to boundary layer meteorology, vol 13. Springer Science & Business Media, Berlin

Tchen CM (1953) On the spectrum of energy in turbulent shear flow. J Res Natl Bur Stand 50(1):51–62

Tchen CM (1954) Transport processes as foundations of the Heisenberg and Obukhoff theories of turbulence. Phys Rev 93(1):4

Tropea C, Yarin AL (2007) Springer handbook of experimental fluid mechanics. Springer Science & Business Media, Berlin

Vallikivi M, Smits AJ (2014) Fabrication and characterization of a novel nanoscale thermal anemometry probe. J Microelectromechanical syst 23(4):899–907

Vallikivi M, Ganapathisubramani B, Smits AJ (2015) Spectral scaling in boundary layers and pipes at very high Reynolds numbers. J Fluid Mech 771:303–326

Wamser C, Peters G, Lykossov VN (1997) The frequency response of sonic anemometers. Bound Layer Meteorol 84(2):231–246

Wyngaard JC (1992) Atmospheric turbulence. Annu Rev Fluid Mech 24(1):205–234

Wyngaard JC, Coté OR (1972) Cospectral similarity in the atmospheric surface layer. Quart J R Meteorol Soc 98(417):590–603

Yavuzkurt S (1984) A guide to uncertainty analysis of hot-wire data. J Fluids Eng 106(2):181–186